Tropical Cyclone Intensification Simulated in the Ooyama-type Three-layer Model with a Multilevel Boundary Layer

Rong Fei[1,2,3] and Yuqing Wang[3*]

[1]State Key Laboratory of Severe Weather, Chinese Academy of Meteorological Sciences, China Meteorological Administration, Beijing, China

[2]College of Earth and Planetary Sciences, University of Chinese Academy of Sciences, Beijing, China

[3]International Pacific Research Center and Department of Atmospheric Sciences, University of Hawaii at Manoa, Honolulu, HI, USA

May 5, 2021 (submitted)
July 27, 2021 (revised)
Dateline

Submitted to ***Journal of the Atmospheric Sciences***

* Corresponding author address:
Prof. Yuqing Wang
International Pacific Research Center
University of Hawaii at Manoa
404A/POST, 1680 East West Road,
Honolulu, HI 96822, USA.
Email: yuqing@hawaii.edu

Abstract

The first successful simulation of tropical cyclone (TC) intensification was achieved with a three-layer model, often named the Ooyama-type three-layer model, which consists of a slab boundary layer and two shallow water layers above. Later studies showed that the use of a slab boundary layer would produce unrealistic boundary layer wind structure and too strong eyewall updraft at the top of TC boundary layer and thus simulate unrealistically rapid intensification compared to the use of a height-parameterized boundary layer. To fully consider the highly height-dependent boundary layer dynamics in the Ooyama-type three-layer model, this study replaced the slab boundary layer with a multilevel boundary layer in the Ooyama-type model and used it to conduct simulations of TC intensification and also compared the simulation with that from the model version with a slab boundary layer. Results show that compared with the simulation with a slab boundary layer, the use of a multilevel boundary layer can greatly improve simulations of the boundary-layer wind structure and the strength and radial location of eyewall updraft, and thus more realistic intensification rate due to better treatments of the surface layer processes and the nonlinear advection terms in the boundary layer. Sensitivity of the simulated TCs to the model configuration and to both horizontal and vertical mixing lengths, sea surface temperature, the Coriolis parameter, and the initial TC vortex structure are also examined. The results demonstrate that this new model can reproduce various sensitivities comparable to those found in previous studies using fully physics models.

1. Introduction

Understanding the dynamics and thermodynamics of tropical cyclone (TC) boundary layer is of great importance to both theoretical research and practical applications. Various boundary layer models have been developed to deal with issues on different aspects of TCs, e.g., column model, depth-averaged (slab) model, and height-resolving model, as summarized in Kepert (2010a). Among these models, the slab model has been widely utilized in various applications because of its simplicity and computational efficiency while it can capture some major features of TC boundary layer. For example, slab boundary layer models have been used in wind engineering (Vickery et al. 2000, 2009a; Williams 2015) and risk assessment of TCs (Powell et al. 2005; Vickery et al. 2009b). The slab boundary layer is also used in understanding the asymmetric structure of a moving TC boundary layer (e.g., Shapiro 1983) and in the three-layer model of TC intensification (Ooyama 1969, hereafter the Ooyama-type model; Schecter 2009, 2011; Frisius and Lee 2016; Lee and Frisius 2018). In addition, the TC potential intensity theory is also based on the slab boundary layer assumption (Emanuel 1988; Bister and Emanuel 1998; Frisius et al. 2013).

Slab boundary layer models have some unavoidable weaknesses in simulating TC boundary layer due to some unphysical simplifications that are inherent to their formation as pointed out by Kepert (2010a,b). For example, in response to a prescribed distribution of pressure gradient force, a slab boundary layer model produces too strong inflow, too strong eyewall updraft, and too great departure from gradient wind balance in TC boundary layer compared to a height-resolving boundary layer model (Kepert 2010a; Williams 2015). These discrepancies result primarily from the use of the depth-averaged boundary layer wind instead of the near-surface wind in calculating surface wind stress (Ooyama 1969; Shapiro 1983) and the ignored vertical structure of boundary-layer winds (Kepert 2010b). The former may considerably overestimate the surface wind stress and enthalpy flux because the near-surface wind speed is often weaker than the depth-averaged wind speed in TC boundary layer (Kepert 2010a). The latter would cause large errors in the calculated tendencies of both tangential and radial winds contributed by the nonlinear advection terms, particularly in the region near and slightly inside the radius of maximum wind (Kepert 2010b).

Frisius and Lee (2016, hereafter FL16) compared the evolutions of TCs simulated in the Ooyama-type three-layer model with a slab boundary layer and a parameterized height-dependent boundary layer proposed by Kepert (2010b). They found that the TC simulated with the slab boundary layer intensified too fast and reached a too strong final intensity compared with that simulated with the parameterized height-dependent boundary layer. This seems to be consistent with the findings of Kepert (2010a) based on a boundary layer model comparison mentioned above because the slab assumption may produce too strong inflow and too strong eyewall updraft. FL16 speculated that the differences in the simulated TC behavior with the two boundary layers could be due to the use of the depth-averaged boundary layer wind velocities in the slab boundary layer and the near-surface wind velocities in the parameterized height-dependent boundary layer in calculating surface wind stress and enthalpy flux.

Note that the parametrized height-dependent boundary layer of Kepert (2010b) was based on some simplifications and was adopted to approximately diagnose the differences in the simulated TC boundary layer between a slab boundary layer model and a fully nonlinear multilevel boundary layer model. Therefore, for a more quantitative comparison of the simulated TC behaviors in the Ooyama-type three-layer model with a slab boundary layer and a height-dependent boundary layer, a fully nonlinear multilevel boundary layer should be used. In addition, since both the surface wind stress and enthalpy flux were overestimated in the simulation with the slab boundary layer, it is unclear whether the differences between the simulations with the slab boundary layer and the parameterized height-dependent boundary layer in FL16 were due to the overestimated surface enthalpy flux or the overestimated surface wind stress or both. In this study, a fully nonlinear multilevel boundary layer is used in the Ooyama-type three-layer model to address the above-mentioned issues.

The main objectives of this study are to extend the Ooyama-type three-layer model with the slab boundary layer to a model with a fully nonlinear multilevel boundary layer, examine the performance of the new model configuration in simulating TC intensification, and compare with the performance with the use of a slab boundary layer. We will also demonstrate through sensitivity experiments that because the multilevel boundary layer avoids some inherent weaknesses of the slab boundary layer, as indicated by Kepert (2010a,b), the Ooyama-type model with the use of a multilevel boundary layer can reproduce TC intensification process comparable with those simulated in full-physics models. The rest of the paper is organized as follows. Model description and experimental design are presented in section 2. In section 3, the TC evolution simulated in the Ooyama-type model with a multilevel boundary layer are discussed and compared with that simulated with a slab boundary layer. The sensitivities of the newly developed Ooyama-type model with the multilevel boundary layer to model configurations, various physical parameters, and the initial vortex structure are discussed in section 4. Finally, major conclusions are summarized and discussed in section 5.

2. Model description and experimental design

The original Ooyama three-layer model Ooyama (1969) used a slab boundary layer and was built under the assumption of gradient wind balance. An extended version with the gradient wind balance assumption removed can be found in FL16, which was used in this study to perform numerical experiments and compare with the simulations with a multilevel boundary layer developed in this study. To facilitate the model description, we start with the version with a slab boundary layer below, which is followed by an introduction of the new version with a multilevel boundary layer and then a description of experimental design.

a. The Ooyama-type model with a slab boundary layer (SBL)

The Ooyama-type three-layer model (hereafter in brief, the Ooyama-type model) with a slab boundary layer used in this study is the same as that described in FL16, which is an extended version of the original Ooyama three-layer model (Ooyama 1969) with the assumption of gradient wind balance removed (hereafter SBL). The three layers are the boundary layer (layer b), the lower free atmosphere (layer 1), and the upper free atmosphere (layer 2). The boundary layer has a fixed depth of h_b and it allows permeation with the two layers above and the exchanges of momentum and heat with the underlying ocean surface. The two layers of the free atmosphere are modeled with two shallow water layers with different densities. The density of the boundary layer and lower layer free atmosphere is ρ_0, and that of the upper layer free atmosphere is $\varepsilon\rho_0$ with $\varepsilon = 0.9$. The axisymmetric assumption is assumed in this study as in FL16 and the governing equations in cylindrical coordinates are as follows:

$$\frac{\partial u_j}{\partial t} + u_j \frac{\partial u_j}{\partial r} - \left(f + \frac{v_j}{r}\right) v_j = -\frac{\partial P_j}{\partial r} + D_{v,u_j} + D_{hd,u_j}, j = 1,2, \tag{1}$$

$$\frac{\partial v_j}{\partial t} + u_j \zeta_j = D_{v,v_j} + D_{hd,v_j}, j = 1,2, \tag{2}$$

$$\frac{\partial u_b}{\partial t} + u_b \frac{\partial u_b}{\partial r} - \left(f + \frac{v_b}{r}\right) v_b = -\frac{\partial P_1}{\partial r} + D_{v,u_b} + D_{hd,u_b} + D_{s,u_b}, \tag{3}$$

$$\frac{\partial v_b}{\partial t} + u_b \zeta_b = D_{v,v_b} + D_{hd,v_b} + D_{s,v_b}, \tag{4}$$

$$\frac{\partial \theta_{e,b}}{\partial t} + u_b \frac{\partial \theta_{e,b}}{\partial r} = D_{v,\theta_{e,b}} + D_{hd,\theta_{e,b}} + D_{s,\theta_{e,b}}, \tag{5}$$

$$\frac{\partial h_1}{\partial t} + \frac{1}{r}\frac{\partial}{\partial r}(r u_1 h_1) = Q_{b,1} - Q_{1,b} - Q_{1,2}, \tag{6}$$

$$\frac{\partial h_2}{\partial t} + \frac{1}{r}\frac{\partial}{\partial r}(r u_2 h_2) = \frac{Q_{b,2}}{\varepsilon} + \frac{Q_{1,2}}{\varepsilon}, \tag{7}$$

$$w_b = -\frac{h_b}{r}\frac{\partial r u_b}{\partial r}, \tag{8}$$

$$P_1 = g(h_1 - H_1) + \varepsilon g(h_2 - H_2), \tag{9}$$

$$P_2 = g(h_1 - H_1) + g(h_2 - H_2), \tag{10}$$

where *r* and *t* are radius and time; u_1 (u_2) and v_1 (v_2) are the radial and tangential winds in layer 1 (layer 2); u_b, v_b, w_b, and *f* are depth-averaged radial wind, tangential wind, vertical velocity at the boundary layer top, and the Coriolis parameter (assumed the value at 20°N except otherwise specified); *P* is kinematic pressure anomaly; $\zeta = f + r^{-1}\partial(rv)/\partial r$ is absolute vertical vorticity; and h_1 and h_2 are the layer depths of the layers 1 and 2, respectively, H_1 and H_2 are their mean layer depths; $\theta_{e,b}$ is the well-mixed equivalent potential temperature in the boundary layer; $Q_{i,j}$ represents the mass flux from layer *i* to layer *j*; $D_{v,X}$, where *X* is *u*, *v*, or θ_e, denotes the vertical exchange of momentum or heat between two neighboring layers and is parameterized with the vertical mass flux; $D_{hd,X}$ means the horizontal diffusion of variable *X*; and $D_{s,X}$ represents the tendency caused by surface momentum or heat exchange.

The mass fluxes ($Q_{1,2}, Q_{b,1}, Q_{b,2}$, and $Q_{1,b}$) between layers due to convection are assumed to be proportional to the upward mass flux from the boundary layer top, which is defined as $Q_b = (w_b + |w_b|)/2$. These mass fluxes are functions of Q_b and the entrainment parameter η, as given in their Eqs. (11)–(13) and (16) in FL16. The entrainment parameter η is a measure for deep convective instability. A transition from shallow to deep convection takes place when η exceeds 1. The surface flux-induced tendencies are parameterized using the bulk aerodynamic formula given below:

$$D_{s,u_b} = -C_D S_b u_b / h_b, \tag{11}$$

$$D_{s,v_b} = -C_D S_b v_b / h_b, \tag{12}$$

$$D_{s,\theta_{e,b}} = -C_E S_b \left(\theta_{e,b} - \theta_{e,s}^*\right) / h_b, \tag{13}$$

where S_b is the surface wind speed calculated using u_b and v_b, $\theta_{e,s}^*$ is the equivalent potential temperature at the given sea surface temperature (SST, which is 29ºC except otherwise specified). The surface drag coefficient C_D is a function of wind speed given as $10^{-3} \times \max\{1.12, min[2.581, 1.0 + 0.06(S_b - 5)]\}$ and the surface exchange coefficient C_E for enthalpy flux is a constant of 1.29×10^{-3}. The horizontal diffusion ($D_{hd,X}$) is formulated as in FL16 [cf. their Eqs. (21)-(23)] but with horizontal diffusion coefficient following the Smagorinsky scheme (Smagorinsky 1963) and the horizontal mixing length l_h of 600 m (except otherwise specified). The vertical exchange terms (D_{v,u_b}, D_{v,v_b}, D_{v,u_1}, D_{v,v_1}, D_{v,u_2}, D_{v,v_2}, and $D_{v,\theta_{e,b}}$) are calculated following FL16 [cf. their Eqs. (24), (25), (28)-(30)].

b. The Ooyama-type model with a multilevel boundary layer (MBL)

In this Ooyama-type model (hereafter, MBL), the slab boundary layer is replaced by a multilevel boundary layer, which is a simplified version of the boundary layer model of Kepert and Wang (2001) and outlined in Li and Wang (2021a) and also used in Fei et al. (2021). Exchanges of mass, momentum and heat between the boundary layer and the two layers above occur at the prescribed boundary layer top h_b, which is set to be 1000 m as in the slab boundary layer. Our tests show that the major results are not strongly dependent on the height of the prescribed boundary layer top in a reasonable range (see discussions in section 4a). The governing equations of the multilevel boundary layer are given below

$$\frac{\partial u}{\partial t}+u\frac{\partial u}{\partial r}+w\frac{\partial u}{\partial z}-\left(f+\frac{v}{r}\right)v=-\frac{\partial P_1}{\partial r}+D_{v,u_b}+D_{hd,u}+D_{vd,u}, \tag{14}$$

$$\frac{\partial v}{\partial t}+u\zeta+w\frac{\partial v}{\partial z}=D_{v,v_b}+D_{hd,v}+D_{vd,v}, \tag{15}$$

$$\frac{\partial w}{\partial z}+\frac{1}{r}\frac{\partial ru}{\partial r}=0 \tag{16}$$

where *u*, *v*, and *w* are the radial and tangential winds, and vertical velocity; $D_{vd,X}$ is vertical diffusion (including surface friction) of *X* (*u*, or *v*) defined as $-\partial F_{vd,X}/\partial z$, in which $F_{vd,X}$ represents vertical turbulent flux; $F_{vd,X}$ above the surface has the form $F_{vd,X}^{z>0}=-K_v\frac{\partial X}{\partial z}$, where the vertical diffusivity has the form $K_v=l_v^2\left[(\frac{\partial u}{\partial z})^2+(\frac{\partial v}{\partial z})^2\right]^{1/2}$ with the vertical mixing length l_v being parameterized as $l_v^{-1}={l_\infty}^{-1}+(\kappa z)^{-1}$ (Blackadar 1962), with the asymptotic mixing length l_∞ being 90 m (except otherwise specified) and the *von Karmen* constant κ being 0.4; $F_{vd,X}$ at the sea surface is parameterized by the bulk aerodynamic formula and has the form $F_{vd,X}^{z=0}=-C_D S_s X_s$ for momentum flux and $F_{vd,\theta_{e,b}}^{z=0}=-C_E S_s\left(\theta_{e,b}-\theta_{e,s}^*\right)$ for enthalpy flux, in which the variable with the subscript 's' means that it is evaluated at 10-m height. Note that u_b, v_b, w_b in the calculations of mass flux ($Q_{i,j}$) and vertical exchange ($D_{v,X}$) in MBL are defined at the prescribed boundary layer top h_b mentioned above rather than the depth-average in the boundary layer. Note also that the equivalent potential temperature is assumed to be well-mixed in the boundary layer in MBL and thus the same budget equation Eq. (5) as in SBL is used.

c. Numerical solution and experimental design

The governing equations are solved numerically. Both SBL and MBL have a uniform radial grid spacing of 1 km, extending from the TC center outward to 2400 km, where an open lateral boundary condition is assumed. The multilevel boundary layer consists of 20 levels in the vertical from the surface to a height of 1774 m, which is higher than the prescribed boundary layer top (h_b) to ensure that a complete boundary layer structure could be fully captured. We will show in section 4a that reasonable changes in the multilevel model top make negligible difference to the simulated TC evolution. The model time integration is accomplished with the alternative use of forward and forward-backward schemes. Most of the model parameters are identical to those used in FL16 except that more realistic surface exchange coefficients and mixing lengths (l_h and l_∞) are used in our model as listed in Table 1.

The initial cyclonic vortex has the radial profile of tangential wind which is slightly modified from that used in Ooyama (1969) and FL16 and it is given below:

$$v_0(\mathrm{r}) = \begin{cases} v_{m0}\dfrac{2(r/r_m)}{1+(r/r_m)^2}, & r \le r_m \\ v_{m0}\dfrac{2(r/r_m)}{1+(r/r_m)^2}e^{-\left(\frac{r-r_m}{r_o}\right)^2}, & r > r_m \end{cases} \tag{17}$$

where v_{m0} and r_m are the maximum tangential wind and the radius of maximum wind. An exponential decay term with r_o of 1000 km is imposed to the original tangential wind outside r_m

so that the tangential wind nearly vanishes at a limited outer radius. A weak tropical depression with v_{m0}= 10 m s^{-1} and r_m= 80 km is assumed in the boundary layer and in the lower layer free atmosphere while there is no flow in the upper layer free atmosphere in all experiments described below. The initial mass field is in gradient wind balance with the given tangential wind.

Three basic experiments were designed to examine and understand the different behaviors of the simulated TC intensification in the Ooyama-type three-layer model with different treatments of the boundary layer. In experiments SBL and MBL, the slab boundary layer and the multilevel boundary layer were used, respectively, with other model settings being default as described above in sections 2a and 2b. In the sensitivity experiment FMBL, a wind factor (*fac*) with value of 0.8 was applied to 10-m radial and tangential winds in the forms of $u_{10}^M = u_{10} * fac$ and $v_{10}^M = v_{10}/fac$ in calculating surface wind stress and enthalpy flux during the integration of MBL model. This means that in FMBL, the 10-m winds (u_{10}, v_{10}) in calculating the surface wind stress and surface enthalpy flux were replaced by the modified winds (u_{10}^M, v_{10}^M), which was used to mimic the boundary layer averaged winds as in the slab boundary layer. The modified wind speed (S_{10}^M) increases correspondingly with an approximation of S_{10}^M=S_{10}/fac because the surface tangential wind is much larger than the radial wind and largely determines the total surface wind speed. Therefore, the modified winds (u_{10}^M, v_{10}^M) lead to increased surface wind stress and enthalpy flux in FMBL. Note that 0.8 for *fac* was chosen based on the ratio between 10-m winds and the boundary-layer mean winds in the inner core of TCs from previous boundary layer models (e.g., Kepert 2010a) and our preliminary tests.

3. TC intensification with different treatments of the boundary layer

a. An overview of the simulated TC with MBL

Before comparing the simulated TCs with different treatments of the boundary layer in the Ooyama-type three-layer model, some basic characteristics of the simulated TC using the newly developed Ooyama-type model with a multilevel boundary layer (i.e., MBL) are presented here first. The evolutions of the storm intensity and various radii regarding wind structures simulated in MBL are shown in Figs. 1a,b. As we can see from Fig. 1a, the maximum tangential wind at lower free atmosphere (v_{1max}) increases from 10 to 60 m s^{-1} in about 3.5 days (84 h) with the most rapid intensification at 46 h of simulation. The simulated TC maintains its intensity after attaining the steady state, which is different from that in Ooyama (1969) (cf. his Fig. 4) who assumed the gradient wind balance even in the boundary layer but is consistent with that in FL16 (cf. their Fig. 4) who included the unbalanced flow as in this study. FL16 found that the assumption of gradient wind balance in the boundary layer would cause the maximum eyewall ascent to occur outside of the radius of maximum gradient wind (RMGW). The latent heat release in the eyewall ascent produces the maximum positive tangential wind tendency outside the RMGW while frictional convergence (represented by the mass fluxes between the middle layer and the boundary layer, see section 2c in FL16 for more information) reduces the tangential wind inside the RMGW. During the initial spinup period (defined as 6-hourly intensity change less than 2 m s^{-1}) when the vortex is weak, the radius of maximum v_1 (abbr. *rmv1*) increases slightly (Fig. 1b). Once entering the primary intensification stage, the inner core starts contracting continuously and the radius of maximum w_b

(abbr. *rmwb*), which approximately presents the location of diabatic heating, is always located inside *rmv1*. The radius of maximum wind maintains at around 30 km after achieving quasi-steady intensity of 60 m s^{-1}, which is comparable to the observed relationship between TC intensity and the radius of maximum wind (Zhang et al. 2020).

The 6-hourly changes of v_1 and *rmv1* are shown in Fig. 1c. We can see that the *rmv1* contraction generally keeps pace with but precedes the storm intensification, with the fastest contraction rate occurring about 6 h earlier than the highest intensification rate. Similar results have been reported in previous observational and numerical studies (Stern et al. 2015; Qin et al. 2016; Li et al. 2019; Wu et al. 2021). With the intensification of the simulated TC, the outer radii of both the hurricane-force and gale-force winds expand radially outward even after the quasi-steady stage is reached. Compared with those in Ooyama (1969), the outward expansion is much slower in our simulation mainly because the removal of the gradient wind balance assumption in our model induces stronger inflow, and thus more absolute angular momentum is transported inward from the outer-core region to accelerate the inner core. Another measure of TC structure is the inflow angle, defined as $\tan^{-1}(u_{10}/v_{10})$ at the location of v_{10max} in the numerical simulation following Bryan et al. (2012). The inflow angle simulated in MBL maintains around 20° during the quasi-steady stage (not shown), which is close to the averaged 23°obtained based on observations from a large database of dropsonde data (Powell et al. 2009).

The radial distributions of some model variables within a radius of 240 km at three selected times are presented in Fig. 2. The three selected times marked in Fig. 1a are 30, 46, 84 h, which indicate the time when the storm just starts its primary intensification stage, intensifies the most rapidly, and reaches the nearly steady-state intensity, respectively. The upper row in Fig. 2, shows the radial profiles of v_1, v_2, and $-u_b$. Generally, the distributions are consistent with the numerical simulations of the original Ooyama model (cf. their Figs. 4,5). However, v_1 simulated in MBL shows an abrupt radial variation inside its maximum during the primary intensification stage (Figs. 2a,b), especially around the time of the most rapid intensification (Fig. 2b). Similar results can be found in those simulated by the Ooyama-type model with the unbalanced slab boundary layer in FL16 (cf. their Fig. 6). The abrupt radial variation in v_1 near the eyewall ascent is mainly related with the narrow ascent updraft in the unbalanced boundary layer, which causes sharp gradient in the positive tangential wind tendency around the eyewall ascent. Such an abrupt radial variation in v_1 is alleviated by the increasing horizontal diffusion when the storm intensifies further towards its quasi-steady state.

The vertical motion at the boundary layer top (w_b) and the entrainment parameter (η) are shown in the lower row in Fig. 2. The storm intensification is accompanied with the enhancement of eyewall updraft and the gradual decrease of convective instability near the eyewall updraft. The w_b and η profiles show some dissimilarities to those shown in Ooyama (1969). There is a weak subsidence just inside the eyewall updraft in the TC simulated in MBL, while no apparent subsidence is shown in the original Ooyama model. By comparing the balanced and unbalanced simulations in FL16, it turns out that the TCs simulated with the unbalanced boundary layer all exhibit obvious subsidence inside the eyewall ascent, like what is shown in Figs. 2d-f. Note that the subsidence inside the eyewall updraft is a common feature in observations and in simulations with full-physics models (e.g., Willoughby 1998; Wang 2001, 2007; Stern et al. 2015). There is a local minimum in the entrainment parameter at the location of the subsidence because of the cold middle-level low entropy air carried downward to the boundary layer by the subsidence. Nevertheless, this narrow weak downdraft with a low entrainment parameter does not have any considerable influence on the intensification processes of the simulated storm.

The above analysis indicates that the Ooyama-type three-layer model with a multilevel boundary layer can capture the main features of TC evolution qualitatively comparable to those simulated in full-physics models or the Ooyama-type three-layer models with the unbalanced boundary layer as discussed in FL16. However, the simulation shows great improvements to those documented in Ooyama (1969), in which the balanced slab boundary layer was used. This suggests that the model we constructed has included the basic processes that control TC intensification, such as the control of eyewall diabatic heating by the boundary layer dynamics and the balanced response of the secondary circulation to diabatic heating in the eyewall updraft and its role in spinning up the primary circulation as recently schematically shown in Li and Wang (2021a). To further demonstrate the superior of the use of a multilevel boundary layer to the use of a slab boundary layer, we compared the simulations between SBL and MBL in the next subsection.

b. Comparison between simulations with SBL and MBL

The performances of the Ooyama-type three-layer models with a slab boundary layer (SBL) and a height-resolving boundary layer (MBL) in simulating TC development are compared in this subsection. The simulation with a modified MBL (FMBL, see section 2c) is also conducted to help understand the differences between the simulations in SBL and MBL. Figure 3 compares the temporal evolutions of the simulated TC intensity and 6-hourly intensification rate (abbr. IR6) in the three experiments (SBL, MBL, and FMBL). The onset of the primary intensification stage [IR6 $\geqslant$2 m s^{-1} $(6h)^{-1}$] in SBL is the earliest among the three experiments, and accordingly, its most rapid intensification also occurs first at 25 h of simulation with the maximum intensification rate up to 15.8 m s^{-1} $(6h)^{-1}$. After around 60 h of simulation, the storm in SBL reaches the quasi-steady intensity of 59.3 m s^{-1}. The most rapid intensification in MBL occurs at 46 h of simulation with the maximum intensification rate of 11.9 m s^{-1} $(6h)^{-1}$, which is about 21 hours later and 25% smaller than that in SBL, respectively. Besides, it takes about 84 h for the storm in MBL to attain its steady-state evolution, about 40% longer than that in SBL. As a simple check on the realism of the model simulation, the intensification rate is compared to that reported in some earlier observational studies. According to the study of Xu et al. (2016) and Xu and Wang (2018a), the observed maximum intensification rate over the North Atlantic and the western North Pacific are roughly 11 and 10 m s^{-1} $(6h)^{-1}$, respectively, for sea surface temperature of 29℃. The observed maximum intensification rate reflects the upper limit of the intensification rate of a real TC under favorable environmental conditions. The maximum intensification rate of 11.9 m s^{-1} $(6h)^{-1}$ simulated in MBL is comparable with that in observations while that of 15.8 m s^{-1} $(6h)^{-1}$ in SBL is too large. With the wind factor introduced to the near-surface winds in calculating surface wind stress and enthalpy flux in FMBL, the onset of the primary intensification stage becomes much earlier with the initial spinup period shortened by 37%, and the maximum intensification rate is 42% higher than that in MBL, but both are comparable to those simulated in SBL. This suggests that the large intensification rate of the storm simulated in experiment SBL results primarily from the overestimated surface wind stress and enthalpy flux due to the use of the boundary-layer mean winds rather than the near-surface winds as used in MBL.

The structural evolutions of the three storms simulated in MBL, SBL, and FMBL are compared in Fig. 4. Note that during the initial spinup stage, the radius of maximum tangential wind in the lower layer (rmv_1) and the radial location of eyewall updraft at the boundary layer top (rmw_b) show some irregular changes, especially in MBL, because the boundary layer is not well developed in the early model integration. With the intensification of the storm and the contraction of rmv_1, eyewall updraft keeps strengthening and rmw_b contracts continuously. In all experiments, the contraction of both rmv_1 and rmw_b stops when the storms reach their quasi-steady stages. The eyewall updraft strengthens much faster and is also much stronger in SBL than in MBL during the primary intensification stage, which corresponds to the much more rapid intensification in SBL. In addition, the inflow angle of the simulated TC in SBL is around 10° during the steady-state (not shown), which is much smaller than that in MBL (20°) and observation (23°). This is because the inflow angle in a slab boundary layer is determined by the boundary-layer averaged tangential and radial winds, namely weaker inflow and stronger tangential wind than those near the surface in MBL. With the surface wind stress and enthalpy flux enhanced in FMBL relative to those in MBL, the eyewall updraft core becomes stronger and is located more inside *rmv1* than that in MBL. This can be clearly seen from the horizontal reference lines in Figs. 4a,c, which mark the model times when the storm intensities in terms of the maximum v_1 are at 15, 20, and 30 m s^{-1}, respectively. The larger diabatic heating rate more inside *rmv1* implies higher heating efficiency and thus higher intensification rate in FMBL than in MBL as inferred from the balanced vortex dynamics (Schubert and Hack 1982; Pendergrass and Willoughby 2009). Similar mechanism applies to the shortened initial spinup period in FMBL compared to that in MBL.

Although the eyewall updraft is about 50% weaker in FMBL than in SBL, the primary intensification of the simulated storm in FMBL starts only several hours later but with the maximum intensification rate slightly higher (Fig. 3). This can be explained by the difference in the locations of the eyewall heating relative to *rmv1*. As we can see from Fig. 4, the updraft core simulated in FMBL is located more inside *rmv1* than that in SBL during the primary intensification stage, implying the higher heating efficiency in FMBL than in SBL. The radial location of the eyewall updraft is determined by the frictional convergence of the boundary-layer inflow. The outwardly located eyewall updraft in SBL relative to that in FMBL results from the weaker overshooting of the boundary-layer inflow, which is presumedly due to the inaccurate calculation of vertically averaged nonlinear advection terms in the slab boundary layer in SBL. Figure 5 compares the true depth-averaged advection term $-\overline{u\partial u/\partial r}$ and the slab-model equivalent advection term $-\overline{u}\,\partial\overline{u}\,/\partial r$ in the boundary layer of MBL. It is clear that the slab-model treatment of the nonlinear advection terms substantially underestimates the magnitude of the negative radial advection of radial wind near the radius of maximum upward motion and shifts the true location of the minimum radial advection of radial wind outward. Namely, the overshooting of the frictional inflow in a slab boundary layer is less inwardly penetrated relative to the RMGW than that in a height-resolving boundary layer. Consistent results were also documented by Kepert (2010b) based on a diagnostic height-resolving boundary layer model. Kepert (2010b) indicated that the errors in calculating the nonlinear advection term in the slab boundary layer are not negligible but are not very large either with an acceleration error of 10^{-4} m s^{-2}. He also mentioned that errors cannot be fully captured based on the budget analysis in a diagnostic model because the slab model is nonlinear and the error may accumulate. The results in our study partly confirm his speculation. Although the acceleration errors of 10^{-3}-10^{-4} m s^{-2} during intensification in this study are not too big in magnitude, they have a persistent and cumulative effect on boundary-layer inflow during TC intensification, which then influences eyewall updraft and intensification rate to some extent. Above-mentioned analysis indicates that the simplification in calculating the nonlinear advection terms in a slab boundary layer can cause non-negligible simulation errors.

Interestingly, although the intensification rate differs greatly among SBL, MBL, and FMBL, the quasi-steady state intensities of the three simulated storms are very close (Fig. 3a). To understand this feature, we conducted two additional sensitivity experiments similar to FMBL to isolate the roles of surface wind stress and surface enthalpy flux in affecting the behavior of the simulated storm. In one experiment (FMBL_heat), the modified winds are only used in calculating surface enthalpy flux, while in the other experiment (FMBL_fric), the modified winds are only used in calculating surface wind stress.

Figure 6 compares the time series of storm intensities and 6-hourly intensification rates simulated in FMBL, FMBL_heat, FMBL_fric, and MBL. The storm simulated in FMBL, in which the modified winds are used in calculating both surface wind stress and surface enthalpy flux, has the shortest initial spinup period, intensifies the most rapidly among the four experiments, and attains the quasi-steady intensity after about 60 h of simulation. With the modified winds only used in calculating surface enthalpy flux in FMBL_heat, the primary intensification stage is substantially delayed compared to that simulated in FMBL but occurs slightly earlier than that in MBL. The storm intensifies less rapidly with the maximum intensification rate reduced by about 18% compared to that simulated in FMBL but somewhat higher than that simulated in MBL. The storm simulated in FMBL_heat reaches its quasi-steady state intensity of 63.0 m s^{-1}, which is about 5% stronger than that simulated in MBL and FMBL. This suggests that surface enthalpy flux contributes positively to both the intensification rate and the final maximum intensity of the simulated storm. Compared to that in FMBL, the primary intensification in FMBL_fric is only slightly delayed but with the maximum intensification rate reduced by about 13%, while the quasi-steady intensity of the storm simulated by FMBL_fric is about 5% weaker than that simulated in MBL and FMBL. This indicates that surface friction can largely shorten the initial spinup period and contributes positively to the intensification rate but limits the final maximum intensity of the simulated TC. These results are generally in agreement with those recently examined by Li and Wang (2021a), who found that increasing surface drag coefficient in a reasonable range shortened the initial spin-up time but reduced the final maximum intensity. In the early spinup period, the large surface wind stress favors the development of boundary layer inflow, and thus the eyewall updraft, leading to the earlier development of eyewall convection and the onset of the primary intensification stage. With the intensification of the storm, the gradually increasing wind speed results in rapidly enhancing surface frictional effect, which increases with the square of surface wind speed, limiting the final maximum intensity of the simulated storm. Although the positive effect from frictionally induced boundary layer convergence and the eyewall updraft also increases as the storm intensifies, its effect is largely offset by the negative effect from the frictional loss of kinetic energy. Eventually, the positive effect of surface enthalpy flux and the negative effect of surface wind stress are almost balanced, leading to little difference in the final intensity among FBML, SBL, and MBL as we can see from Fig. 3a.

The above results, however, differ from those in FL16, who found that the storm simulated in the Ooyama-type model with a slab boundary layer was substantially stronger in the quasi-steady stage than that simulated with a parameterized height-dependent boundary layer (cf. their Fig. 4), as also mentioned in the introduction. The difference is probably caused by the intrinsic weaknesses of the parameterized height-dependent boundary layer model in simulating the boundary layer structure as shown in Kepert (2010b). He compared the boundary-layer wind structures simulated in the parameterized height-dependent and the multilevel height-resolving boundary layer models. With the same other model settings, the parameterized height-dependent boundary layer model simulated upward motion about 30% weaker than the multilevel height-resolving boundary layer model. The too weak eyewall updraft in the parameterized height-dependent boundary layer model could be related to the fixed constant boundary layer depth and the simplified treatment of vertical advection term. As a result, with similar surface wind stress, weaker upward motion and thus convective heating in the eyewall in the simulation with the parameterized height-dependent boundary layer may lead to a weaker maximum steady-state intensity. Therefore, the weaker final maximum intensity of the storm simulated with the parameterized height-dependent boundary layer than that simulated with the slab boundary layer in FL16 could be due to the intrinsic weakness of the parameterized height-dependent boundary layer, which underestimates the final maximum intensity of the simulated storm.

4. Sensitivity experiments with MBL

In this section, the good performance of the newly developed Ooyama-type model with a multilevel boundary layer (MBL) is demonstrated with various sensitivity experiments, including those previously studied with full-physics models in the literature. Three groups of experiments are considered. In the first group, the sensitivity of the simulated storm to the model configuration, including the selected model depth and boundary layer top, is conducted to demonstrate that our main results and conclusions are little dependent on the model configuration. In the second group, the sensitivity of the simulated storm to several key physical parameters, including the sea surface temperature, latitude, and both horizontal and vertical mixing lengths, is examined to demonstrate that the simple model can reproduce most of the features that are previously simulated with full-physics models. In the third group, the sensitivity of the simulated storm to the initial vortex structure, including the radius of maximum wind and the decaying rate of tangential wind outside the radius of maximum wind, is examined to demonstrate that the simple model can duplicate the dependence of the simulated TC behavior on the initial TC vortex structure previously simulated with full-physics models in the literature.

a. Sensitivity to model configuration

As in Kepert and Wang (2001), a Neumann boundary condition is used at the top of the multilevel boundary layer described in section 2b, where the vertical gradient of horizontal winds is assumed to be zero. Kepert (2017) demonstrated in his appendix that under the Neumann upper boundary condition, the boundary layer wind structure is insensitive to the height of the model top in a multilevel boundary layer model forced by the prescribed pressure gradient force. Here, the sensitivity of the simulated TC intensification to the model top of the multilevel boundary layer is evaluated in the Ooyama-type three-layer model. We conducted experiments in MBL with various model tops at 1,239 m (16 model levels), 1,774 m (20 levels), and 2,383 m (24 levels), respectively, among which 20 levels is the default setting used elsewhere in the text and the other two are used as sensitivity experiments. In the first sensitivity experiment, 1239 m with 16 vertical levels is marginally higher than h_b, which denotes the boundary layer top where the exchange with the free atmosphere above occurs and is set to be 1000 m in this study (see section 2b). The second sensitivity experiment has 24 vertical levels with the top at 2383 m to ensure that the simulated interior is less affected by the upper boundary condition and a full gradient wind adjustment in the upper part can be achieved. As shown in Fig. 7a, experiments with three different vertical levels simulate almost the same intensification rate and final maximum intensity. This is mainly due to the fact that the simulated boundary layer flow is almost identical (Fig. 8), as demonstrated in the forced boundary layer model by Kepert (2017). Therefore, choosing different model levels for the multilevel boundary layer has little influence on the behavior of the simulated TC in MBL.

Another model configuration in MBL is related to the definition of the boundary layer top (h_b), which is set to be 1000 m by default, the same as that used in SBL. In the assumed slab boundary layer, turbulence mixing is presumed to vanish at the boundary layer top. However, this assumption cannot be fully satisfied in the multilevel boundary layer because the vertical diffusion is not necessarily zero above h_b. In addition, choosing different boundary layer depths may affect the updraft at the boundary layer top and also the equivalent potential temperature in the boundary layer. Therefore, we further examined whether the chosen boundary layer depth has a significant impact on the simulated TC. Three experiments with the boundary layer tops at 782 m (at the 12th level), 1000 m (at the 14th level), and 1239 m (at the 16th level), respectively, were conducted. Figure 7b shows that with a reduced boundary layer depth, the initial spinup period is slightly shortened. This is mainly because the eyewall updraft below 1000 m is located slightly more radially inward than that at and above 1000 m due to the outward tilt of the eyewall updraft in the boundary layer (see horizontal reference lines in Fig. 8b). This results in relatively higher heating efficiency, and thus the reduced initial spinup period but little effect on the final maximum intensity. Nevertheless, in general, the overall behavior of the simulated storm in MBL is not very sensitive to the chosen boundary layer top at around 1000 m.

b. Sensitivity to physical parameters

The development of a TC is controlled by a series of physical processes, including the turbulent flux at the sea surface, turbulent vertical mixing in the boundary layer, and subgrid scale horizontal diffusion, and so on. It is necessary for a newly developed model (MBL) to be able to capture the sensitivity of the simulated TC to these physical processes consistent with more physically based full-physics models. In other words, the new model should have appropriate response to the varying physical parameters. Therefore, we tested the sensitivity of the simulated TC to various physical parameters, including horizontal mixing length (l_h), asymptotic vertical mixing length (l_∞), SST, and the Coriolis parameter (latitude).

The horizontal and asymptotic vertical mixing lengths control the horizontal and vertical turbulent diffusion, respectively. As shown in Figs. 9a,b, both the maximum intensification rate and the final maximum intensity are highly sensitive to the horizontal mixing length. With the reduced horizontal mixing length (and thus the reduced horizontal diffusion), the simulated storm intensifies more rapidly and reaches a higher final maximum intensity (Fig. 9a), which is consistent with the results in Bryan and Rotunno (2009) and Bryan (2012). Rotunno and Bryan (2012) found that the horizontal diffusion is a major contributor to the angular momentum budget in the inner-core boundary layer and it acts to reduce the angular momentum of the parcels there, thus diffusing the radial distribution of angular momentum carried upward. Note that when l_h is set to 50 m, the TC intensity exhibits some small-scale oscillations, which could be related to the severe frontal discontinuity between the eye and eyewall regions due to the insufficient horizontal mixing across the radius of maximum wind. Different from the horizontal mixing length, the asymptotic vertical mixing length has a relatively weaker influence on the simulated storm. Generally, reducing the asymptotic vertical mixing length results in the reduced intensification rate and final maximum intensity but the impact is rather marginal. Rotunno and Bryan (2012) also found that vertical diffusion hardly influences the maximum tangential wind but it imposes significant effects on the boundary layer depth and the amount of supergradient wind (maximum wind in excess of the gradient wind).

The SST is well recognized as an important factor controlling TC development because it largely determines the energy supply to TCs through surface enthalpy flux from the underlying ocean. With a higher SST, the simulated TC in MBL intensifies more rapidly and attains a higher final maximum intensity (Fig. 9c). This is in agreement with observations and high-resolution numerical simulations by full-physics models (e.g., Xu and Wang 2018a; Črnivec et al. 2016; Li et al. 2020). Note that since the stratification in the free atmosphere above the boundary layer is the same in all SST experiments, the actual comparison is not straightforward.

The Coriolis parameter is another factor that may affect TC intensification rate and the final maximum intensity. Figure 9d shows results from simulations with the Coriolis parameters at different latitudes. We can see that at the lower latitude with a smaller Coriolis parameter or weaker ambient rotation, the simulated storm has higher intensification rate and stronger final maximum intensity. Several previous studies with numerical simulations also reported similar results (DeMaria and Pickle 1988; Smith et al. 2011). Smith et al. (2015) explained such a sensitivity to the dependence of the dynamics of the frictional boundary layer to the Coriolis parameter. Namely, with a reduced Coriolis parameter, the boundary layer inflow and thus the eyewall updraft would be stronger, leading to stronger diabatic heating and thus more rapid intensification and higher final maximum intensity of the simulated storm.

c. Sensitivity to initial vortex structure

In addition to physical parameters, the structure of the TC vortex itself also largely influences its intensification and maximum intensity (Carrasco et al. 2014; Xu and Wang 2015; 2018a,b; Tao et al. 2020; Li and Wang 2021b). For example, the intensification rate of the observed TCs is found to be negatively correlated with the radius of maximum wind and the outer-core wind skirt (Carrasco et al. 2014; Xu and Wang 2015; 2018a). This phenomenon was upheld later by numerical experiments with cloud-resolving models (Xu and Wang 2018b; Tao et al. 2020; Li and Wang

2021b). Previous studies also reported that the final maximum intensity of a numerically simulated TC is positively correlated with the initial inner-core size of a TC (Xu and Wang 2018b; Tao et al. 2020). To see whether the newly developed simple model can reproduce the observed and numerically simulated relationship between the initial TC structure and the subsequent TC intensification and the final maximum intensity, we conducted some sensitivity experiments by varying the radius of maximum wind (r_m) and the decay parameter (r_o) in the initial wind profile given in Eq. (17). The radial distributions of the initial tangential winds used in various experiments are plotted in the thumbnail figures of Figs. 9e, f, from which we can see that vortex with smaller r_m and r_o has a smaller inner-core size and a narrower outer-core wind skirt, respectively.

Consistent with previous studies, the initial spinup period is shorter and the intensification rate during the subsequent primary intensification stage is larger for the vortex with initially smaller r_m and r_o. This has been explained based on the balanced vortex dynamics in Xu and Wang (2018b) and by the dependence of the unbalanced boundary layer dynamical response to the vortex structure in Li and Wang (2021b). According to the balanced vortex dynamics, the vortex initially with a larger r_m (larger r_o) has lower inertial stability inside r_m (higher inertial stability outside r_m). The larger r_m implies smaller eyewall heating efficiency in spinning up the tangential wind in the inner core and the larger r_o implies larger resistance to the inflow into the inner core. Li and Wang (2021b) demonstrated that both the strength and the radial location of diabatic heating in the eyewall depend on the response of the unbalanced boundary layer dynamics, and such a response is greatly controlled by the TC vortex structure and can help explain well the dependence of the simulated TC behavior on the initial TC vortex structure.

Although TCs with an initially smaller r_m or initially narrower outer-core wind skirt intensify more rapidly, they tend to achieve lower final maximum intensities (Figs. 9e,f), consistent with the results in Xu and Wang (2018b). Similar results have also been reported in Tao et al. (2020), who found a linear relationship between r_m and the absolute angular momentum passing through r_m in the simulated steady-state TCs. As they mentioned, their finding suggests that the TC vortex with initially large absolute angular momentum (i.e., larger r_m and/or higher intensity) would be more intense in the steady-state in their model simulations. However, the precise mechanisms are still an issue to be addressed in future studies.

Finally, it is our interest to compare the responses to various parameters in SBL with those in MBL discussed above, corresponding sensitivity experiments (except for the asymptotic vertical mixing length l_∞) using SBL are also conducted with the results compared in Fig. 9. In general, the sensitivities in SBL are consistent with those in MBL. Namely, the Ooyama-type model coupled with the slab boundary layer also responds appropriately to various parameters. However, compared with that in MBL, the intensification in SBL is systematically too rapid. In addition, the TC intensity simulated in SBL exhibits a more obvious instability than that in MBL when the horizontal diffusion is too weak (cf. Fig. 9a where l_h is set to 50 m). This is supposed to be related to the more abrupt radial variation of quantities around the eyewall updraft in SBL.

The above results strongly suggest that the newly developed Ooyama-type model with a multilevel boundary layer can well capture the key dynamical/physical processes responsible for TC intensification and steady-state maximum intensity. It produces more reasonable TC intensification rate and causes less instability than the version with a slab boundary layer when the horizontal diffusion is relatively weak. Although the new model exhibits some sensitivity to the chosen boundary layer top, the sensitivity is marginal with the height in a reasonable range. Therefore, this model can be used in future studies to help understand some basic dynamics in TC intensification and maximum intensity, in particular for those related to the coupling between the boundary layer and the free atmosphere above.

5. Conclusions and discussion

The three-layer model originally developed by Ooyama (1969) is the first numerical model that successfully simulated many aspects of TCs. The Ooyama-type model consists of a slab boundary layer and two shallow water layers above. Later studies showed that the use of a slab boundary layer would produce unrealistic boundary layer wind structure (Kepert 2010a,b; Williams 2015) and too strong eyewall updraft at the top of TC boundary layer and thereby simulate unrealistically rapid intensification compared to the use of a parameterized height-dependent boundary layer (FL16). To fully consider the height-dependent boundary layer dynamics in the Ooyama-type three-layer model, this study replaced the slab boundary layer with a fully nonlinear multilevel boundary layer, performed simulations of TC evolution, and compared the behavior of the simulated TC in the same model settings but with a slab boundary layer.

Results show that compared with the simulation with a slab boundary layer, the use of a fully nonlinear multilevel boundary layer can greatly improve simulations of the boundary-layer wind structure and the strength and radial location of eyewall updraft, and thus more realistic intensification rate to a certain extent. The storm simulated with the multilevel boundary layer experienced a much longer (40%) initial spinup period and lower intensification rate (25%) than that simulated with the slab boundary layer. The improvement results partly from the better treatment for surface wind stress and surface enthalpy flux calculations and partly from the more accurate representation of nonlinear advection terms in the boundary layer. We showed that increasing surface wind stress led to the shortened initial spinup period and thus the earlier onset of the primary intensification stage but a reduced steady-state intensity while increasing surface enthalpy flux led to a marginally earlier onset of the primary intensification stage, a relatively higher intensification rate, and a larger steady-state intensity of the simulated storm. These are consistent with previous results based on fully-physics cloud-resolving model simulations (e.g., Li and Wang 2021a). Further analysis showed that the eyewall updraft in the simulation with the multilevel boundary layer is much weaker but more inside the radius of maximum wind than that in the simulation with the slab boundary layer. This indicates that the weaker diabatic heating with the multilevel boundary layer due to the weaker eyewall updraft is partly compensated by the higher heating efficiency due to higher inertial stability as implied by balanced vortex dynamics. The less inwardly displaced eyewall updraft relative to the radius of maximum wind in the slab boundary layer than in the multilevel boundary layer is partly due to the inaccurate representation of nonlinear advection terms in the slab boundary layer, an intrinsic weakness as revealed by Kepert (2010b).

To further demonstrate the simulation ability of the newly developed simple model, we also performed a series of sensitivity experiments. Results confirmed that our main results and conclusions are little dependent on the model configuration, including the height of the vertical extent of the multilevel boundary layer and the prescribed height of the boundary layer top. In addition, the model can reproduce the TC evolution and sensitivity to various physical parameters and the initial vortex structure comparable to full-physics models reported in the literature.

Finally, we should point out that although the model documented in this study can reproduce many aspects of TCs comparable to those simulated in full-physics models, because of the heavy simplification, most of the results are mainly qualitatively consistent, and close quantitative comparisons may not be straightforward. Some intrinsic weaknesses also exist in such a three-layer configuration, including the oversimplified convective processes (e.g., neglect of the mass ventilation caused by convection) and the upright eyewall structure. Therefore, caution needs to be given when the model simulations are used to explain more complicated physical processes. Nevertheless, the Ooyama-type three-layer model with a multilevel boundary layer designed in this study is highly efficient and captures the basic dynamics of TC intensification processes involving the nonlinear interaction between the boundary layer and free atmosphere above. Therefore, this simple model has the potential to be used in future studies to help understand some basic dynamics in TC intensification and maximum intensity. Besides, the simplicity of the model allows the model to be run easily as an educational tool for class teaching. In addition, only results from the axisymmetric configuration are reported in this study. The behavior of the simulated TC in three-dimensions will be examined in a future work.

Acknowledgments: This study has been supported in part by the National Natural Science Foundation of China under Grant 41730960, and in part by the NSF Grant AGS-1834300. R. Fei is funded by China Scholarship Council (File 201905330037).

References

Bister, M., and K. A. Emanuel, 1998: Dissipative heating and hurricane intensity. *Meteor. Atmos. Phys.*, **52**, 233-240, https://doi.org/10.1007/BF01030791.

Blackadar, A. K., 1962: The vertical distribution of wind and turbulent exchange in a neutral atmosphere. *J. Geophys. Res.*, **67**, 3095–3102, https://doi.org/10.1029/JZ067i008p03095.

Bryan, G. H., and R. Rotunno, 2009: The maximum intensity of tropical cyclones in axisymmetric numerical simulations. *Mon. Wea. Rev*, **137**, 1770-1789, https://doi.org/10.1175/2008MWR2709.1.

Bryan, G. H., 2012: Effects of surface exchange coefficients and turbulence length scales on the intensity and structure of numerically simulated hurricanes. *Mon. Wea. Rev*, **140**, 1125-1143, https://doi.org/10.1175/MWR-D-11-00231.1.

Carrasco, C., C. Landsea, and Y. Lin, 2014: The influence of tropical cyclone size on its intensification. *Wea. Forecasting*, **29,** 582–590, https://doi.org/10.1175/WAF-D-13-00092.1.

Črnivec, N., R. K. Smith, and G. Kilroy, 2016: Dependence of tropical cyclone intensification rate on sea-surface temperature. *Quart. J. Roy. Meteor. Soc*., **142**, 1618–1627, https://doi.org/10.1002/qj.2752.

DeMaria, M., and J. D. Pickle, 1988: A simplified system of equations for simulation of tropical cyclones. *J. Atmos. Sci.*, **45**, 1542–1554, https://doi.org/10.1175/1520-0469(1988)045<1542:ASSOEF>2.0.CO;2.

Emanuel, K. A., 1988: The maximum intensity of hurricanes. *J. Atmos. Sci.*, **45**, 1143–1155, https://doi.org/10.1175/1520-0469(1988)045<1143:TMIOH>2.0.CO;2.

Fei, R., Y. Wang, and Y. Li, 2021: Contributions of vertical advection to supergradient wind in tropical cyclone boundary layer: A numerical study. *J. Atmos. Sci.*, **78**, 1057–1073, https://doi.org/10.1175/JAS-D-20-0075.1.

Frisius, T., D. Schönemann, and J. Vigh, 2013: The impact of gradient wind imbalance on potential intensity of tropical cyclones in an unbalanced slab boundary layer model. *J. Atmos. Sci.*, **70**, 1874–1890, https://doi.org/10.1175/JAS-D-12-0160.1.

Frisius, T., and M. Lee, 2016: The impact of gradient wind imbalance on tropical cyclone intensification within Ooyama's three-layer model. *J. Atmos. Sci.*, **73**, 3659–3679, https://doi.org/10.1175/JAS-D-15-0336.1.

Kepert, J., and Y. Wang, 2001: The dynamics of boundary layer jets within the tropical cyclone core. Part II: Nonlinear enhancement. *J. Atmos. Sci.*, **58**, 2485–2501, https://doi.org/10.1175/1520-0469(2001)058<2485:TDOBLJ>2.0.CO;2.

Kepert, J. D., 2010a: Slab- and height-resolving models of the tropical cyclone boundary layer. Part I: Comparing the simulations. *Quart. J. Roy. Meteor. Soc.*, **136**, 1686–1699, https://doi.org/10.1002/qj.667.

Kepert, J. D., 2010b: Slab- and height-resolving models of the tropical cyclone boundary layer. Part II: Why the simulations differ. *Quart. J. Roy. Meteor. Soc.*, **136**, 1700–1711, https://doi.org/10.1002/qj.685.

Kepert, J. D., 2017: Time and space scales in the tropical cyclone boundary layer, and the location of the eyewall updraft. *J. Atmos. Sci.*, **74**, 3305–3323, https://doi.org/10.1175/JAS-D-17-0077.1.

Lee, M., and T. Frisius, 2018: On the role of convective available potential energy (CAPE) in tropical cyclone intensification. *Tellus*, **70A**, 1-18, https://doi.org/10.1080/16000870.2018.1433433.

Li, Y., Y. Wang, and Y. Lin, 2019: Revisiting the dynamics of eyewall contraction of tropical cyclones. *J. Atmos. Sci.*, **76**, 3229–3245, https://doi.org/10.1175/JAS-D-19-0076.1.

Li, Y.-L. Y. Wang, Y.-L, Lin, and R. Fei, 2020: Dependence of superintensity of tropical cyclones on SST in axisymmetric numerical simulations. *Mon. Wea. Rev.*, **148**(12), 4767–4781, https://doi.org/10.1175/MWR-D-20-0141.1.

Li, T.-H., and Y. Wang, 2021a: The role of boundary layer dynamics in tropical cyclone intensification. Part I: Sensitivity to surface drag coefficient. *J. Meteor. Soc. Japan*, **99**, 537–554, https://doi.org/10.2151/jmsj.2021-027.

Li, T.-H., and Y. Wang, 2021b: The role of boundary layer dynamics in tropical cyclone intensification. Part II: Sensitivity to initial vortex structure. *J. Meteor. Soc. Japan*, **99**, 555–

573, https://doi.org/10.2151/jmsj.2021-028.

Ooyama, K. V., 1969: Numerical simulation of the life cycle of tropical cyclones. *J. Atmos. Sci.*, **26**, 3–40, https://doi.org/10.1175/1520-0469(1969)026<0003:NSOTLC>2.0.CO;2.

Pendergrass, A. G., and H. E. Willoughby, 2009: Diabatically induced secondary flows in tropical cyclones. Part I: Quasi-steady forcing. *Mon. Wea. Rev.*, **137**, 805–821, https://doi.org/10.1175/2008MWR2657.1.

Powell, M. D., G. Soukup, S. Cocke, S. Gulati, N. Morisseau-Leroy, S. Hamid, N. Dorst, and L. Axe, 2005: State of Florida hurricane loss prediction model: Atmospheric science component. *J. Wind Eng. Ind. Aerodyn.*, **93**, 651–674, https://doi.org/10.1016/j.jweia.2005.05.008.

Powell, M. D., E. W. Uhlhorn, and J. D. Kepert, 2009: Estimating maximum surface winds from hurricane reconnaissance measurements. *Wea. Forecasting*, **24**, 868–883, https://doi.org/10.1175/2008WAF2007087.1.

Qin, N., D.-L. Zhang, and Y. Li, 2016: A statistical analysis of steady eyewall sizes associated with rapidly intensifying hurricanes. *Wea. Forecasting*, **31**, 737–742, https://doi.org/10.1175/ WAF-D-16-0016.1.

Rotunno R., and G. H. Bryan, 2012: Effects of parameterized diffusion on simulated hurricanes. *J. Atmos. Sci.*, **69**, 2284–2299, https://doi.org/10.1175/JAS-D-11-0204.1.

Schecter, D. A., and T. J. Dunkerton, 2009: Hurricane formation in diabatic Ekman turbulence. *Quart. J. Roy. Meteor. Soc.*, **135**, 823–838, https://doi.org/10.1002/qj.405.

Schecter, D. A., 2011: Evaluation of a reduced model for investigating hurricane formation from turbulence. *Quart. J. Roy. Meteor. Soc.*, **137**, 155–178, https://doi.org/10.1002/qj.729.

Schubert, W. H., and J. J. Hack, 1982: Inertial stability and tropical cyclone development. *J. Atmos. Sci.*, **39**, 1687-1697, https://doi.org/10.1175/1520-0469(1982)039<1687:ISATCD>2.0.CO;2.

Shapiro, L. J., 1983: The asymmetric boundary layer flow under a translating hurricane. *J. Atmos. Sci.*, **40**, 1984–1998, https://doi.org/10.1175/1520-0469(1983)040<1984:TABLFU>2.0.CO;2.

Smith, R. K., C. W. Schmidt, and M. T. Montgomery, 2011: An investigation of rotational influences on tropical-cyclone size and intensity. *Quart. J. Roy. Meteor. Soc.*, **137**, 1841–1855, https://doi.org/10.1002/qj.862.

Smith, R. K., G. Kilroy, and M. K. Montgomery, 2015: Why do model tropical cyclones intensify more rapidly at low latitudes. *J. Atmos. Sci.*, **72**, 1783–1804, https://doi.org/10.1175/JAS-D-14-0044.1.

Stern, D. P., J. L. Vigh, D. S. Nolan, and F. Zhang, 2015: Revisiting the relationship between eyewall contraction and intensification. *J. Atmos. Sci.*, **72**, 1283–1306, https://doi.org/10.1175/JAS-D-14-0261.1.

Tao, D., M. Bell, R. Rotunno, and P. J. Van Leeuwen, 2020: Why do the maximum intensities in modeled tropical cyclones vary under the same environmental conditions? *Geophys. Res. Lett.*, **47**, e2019GL085980, https://doi.org/10.1029/2019gl085980.

Vickery, P. J., P. F. Skerlj, A. C. Steckley, and L. A. Twisdale, 2000: Hurricane wind field model for use in hurricane simulations. *J. Struct. Eng.*, **126**, 1203–1221, https://doi.org/10.1061/(ASCE)0733-9445(2000)126:10(1203).

Vickery, P. J., D. Wadhera, M. D. Powell, and Y. Chen, 2009a: A hurricane boundary layer and wind field model for use in engineering applications. *J. Appl. Meteor. Climatol.*, **48**, 381–405, https://doi.org/10.1175/2008JAMC1841.1.

Vickery, P. J., F. J. Masters, M. D. Powell, and D. Wadhera, 2009b: Hurricane hazard modeling: The past, present, and future. *J. Wind Eng. Ind. Aerodyn.*, **97**, 392–405, https://doi.org/10.1016/j.jweia.2009.05.005.

Wang, Y., 2001: An explicit simulation of tropical cyclones with a triply nested movable mesh primitive equation model: TCM3. Part I: Model description and control experiment. *Mon. Wea. Rev***., 129,** 1370-1394, https://doi.org/10.1175/1520-0493(2001)129<1370:AESOTC>2.0.CO;2.

Wang, Y., 2007: A multiply nested, movable mesh, fully compressible, nonhydrostatic tropical cyclone model - TCM4: Model description and development of asymmetries without explicit asymmetric forcing. *Meteor. Atmos. Phys.*, **97,** 93-116. https://doi.org/10.1007/s00703-006-0246-z.

Williams, G. J., 2015: The effects of vortex structure and vortex translation on the tropical cyclone boundary layer wind field. *J. Adv. Model. Earth Syst.*, **7**, 188–214, https://doi.org/10.1002/2013MS000299.

Willoughby, H. E, 1998: Tropical cyclone eye thermodynamics. *Mon. Wea. Rev*., **126**, 3053–3067, https://doi.org/10.1175/1520-0493(1998)126,3053:TCET.2.0.CO;2

Wu, Q., and Z. Ruan, 2021: Rapid contraction of the radius of maximum tangential wind and rapid intensification of a tropical cyclone. *J. Geophys. Res. Atmos.*, **126**, e2020JD033681, https://doi.org/10.1029/2020JD033681.

Xu, J., and Y. Wang, 2015: A statistical analysis on the dependence of tropical cyclone intensification rate on the storm intensity and size in the North Atlantic. *Wea. Forecasting*, **30**, 692–701, https://doi.org/10.1175/WAF-D-14-00141.1.

Xu, J., Y. Wang, and Z. M. Tan, 2016: The relationship between sea surface temperature and maximum intensification rate of tropical cyclones in the North Atlantic. *J. Atmos. Sci.*, **73**, 4979–4988, https://doi.org/10.1175/JAS-D-16-0164.1.

Xu, J., and Y. Wang, 2018a: Dependence of tropical cyclone intensification rate on sea surface temperature, storm intensity and size in the western North Pacific. *Wea. Forecasting*, **33(2)**, 523–537, https://doi.org/10.1175/WAF-D-17-0095.1

Xu, J., and Y. Wang, 2018b: Effect of the initial vortex structure on intensification of a numerically simulated tropical cyclone. *J. Meteor. Soc. Japan*. **96**, 111–126, https://doi.org/10.2151/jmsj.2018-014.

Zhang, G., W. Perrie, B. Zhang, J. Yang, and Y. He, 2020: Monitoring of tropical cyclone structures in ten years of RADARSAT-2 SAR images. *Remote Sens. Environ*., **236**, https://doi.org/10.1016/j.rse.2019.111449.

Table 1. Values of model parameters.

Parameter	Value
ε	0.9
h_b	1000 m
H_1, H_2	5000 m
f	$5 \times 10^{-5}\ s^{-1}$ (latitude: 20°N)
$\overline{\theta_{e,s}^{*}}$	372 K (sea surface temperature: 29℃)
$\theta_{e,1}$	332 K
$\overline{\theta_{e,2}^{*}}$	342 K
a	$0.001\ K\ s^2 m^{-2}$
b	$0.0002\ K\ s^2 m^{-2}$
l_h	600 m
l_v	90 m
C_E	1.29×10^{-3}

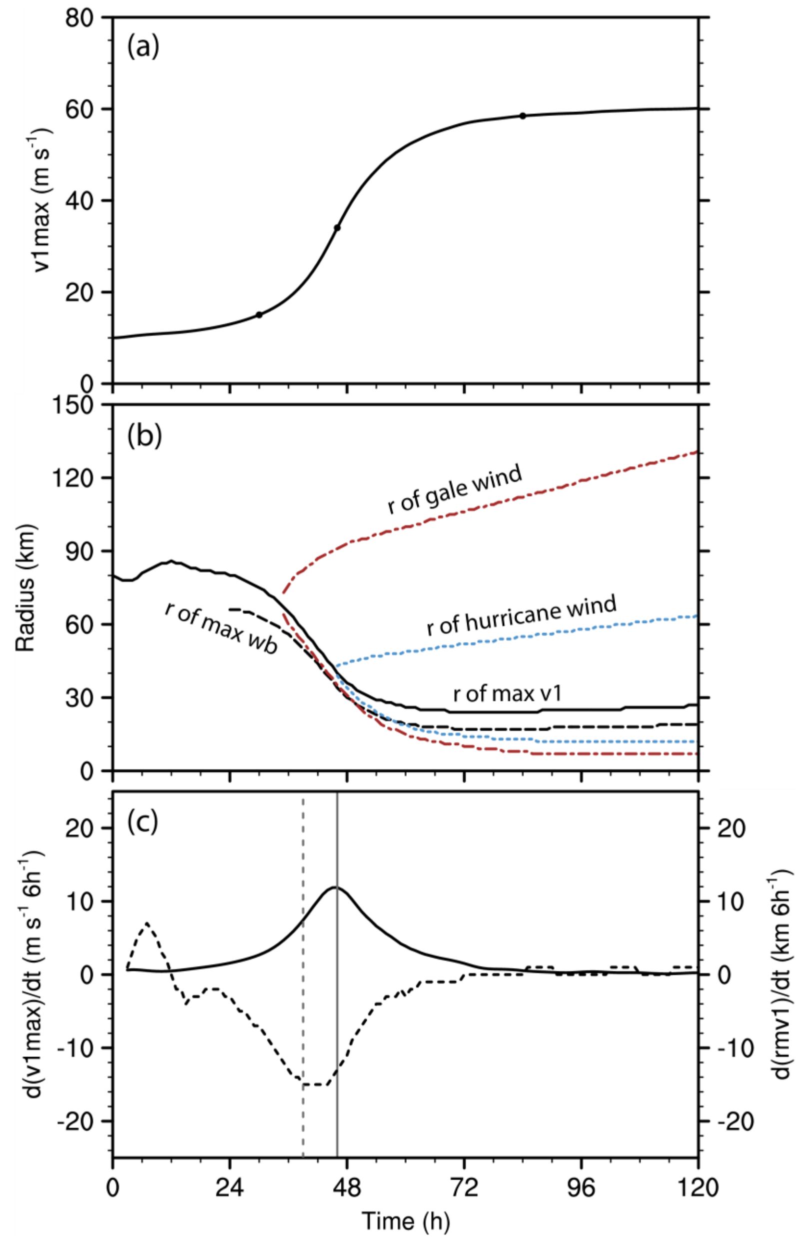

Fig. 1. Evolution of the simulated TC in MBL: (a) maximum v_1; (b) radii of maximum v_1, maximum w_b, and outer and inner limits of hurricane- and gale-force winds; (c) 6-hourly change of maximum v_1 (solid, left coordinate) and radius of maximum v_1 (dashed, right coordinate). Dots on the curve in (a) indicate the times selected for the detailed illustration in Fig. 2. Solid and dashed vertical reference lines in (c) denote time of the most rapid intensification rate and the time of the fastest contraction of radius of maximum v_1, respectively.

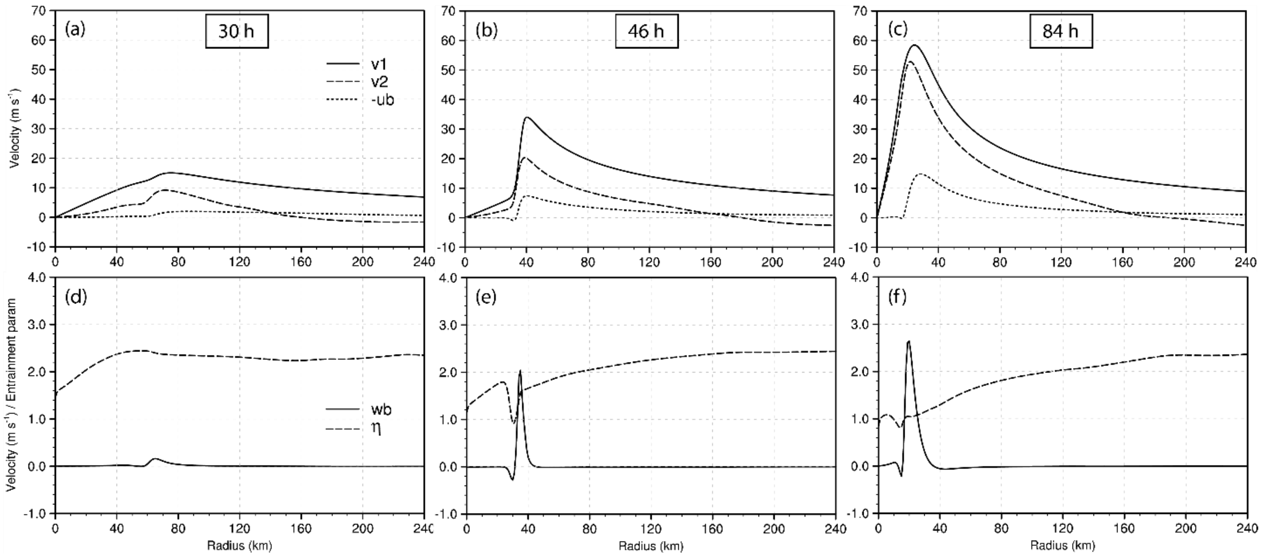

Fig. 2. Radial distributions of various variables within a radius of 240 km in the simulated TC in MBL at t=30, 44, and 84 h, including v_1, v_2, and u_b (upper panels) and w_b and η (lower panels).

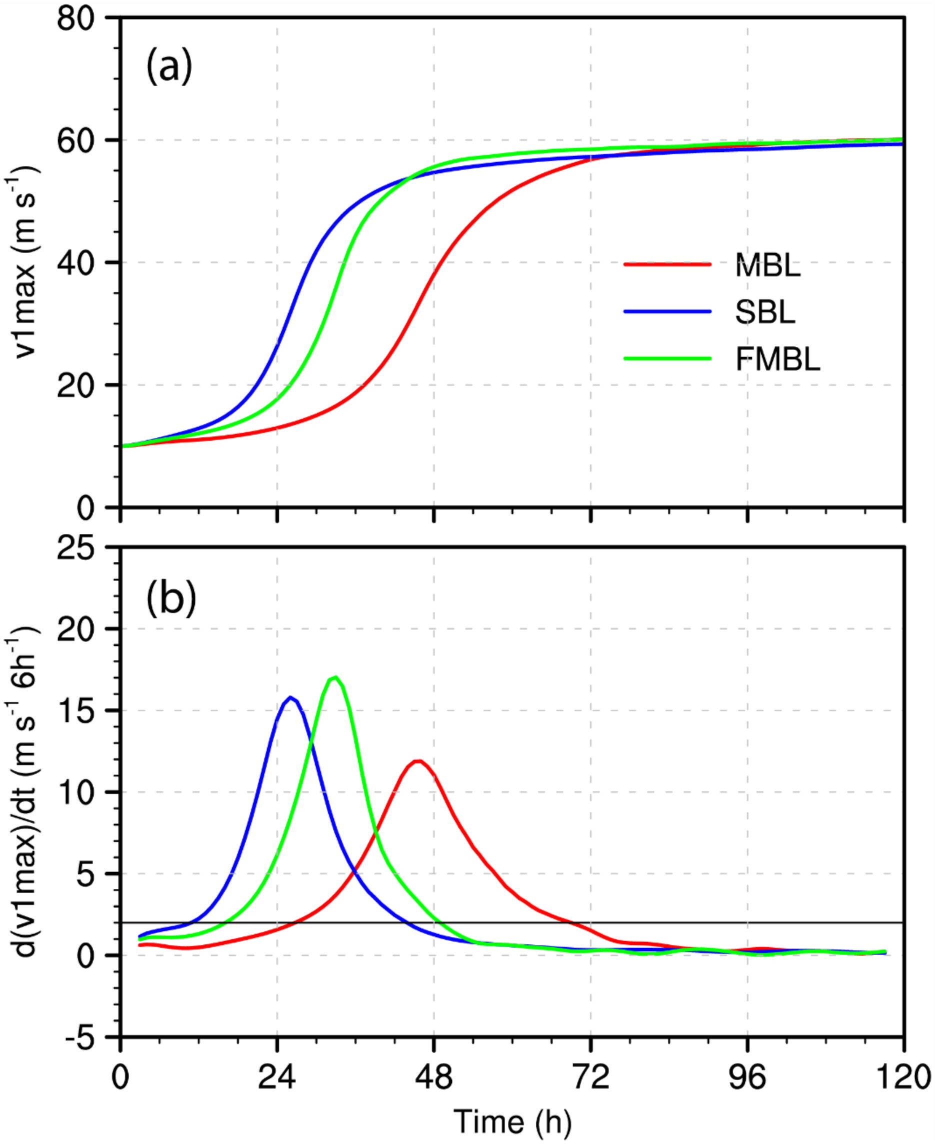

Fig. 3. Time series of (a) maximum v_1 and (b) 6-hourly intensification rate (IR6) in MBL (red), SBL (blue), and FMBL (green). The horizontal line in (b) denotes the intensification rate of 2 m s^{-1} $(6h)^{-1}$, which is deemed as the onset of the primary intensification phase.

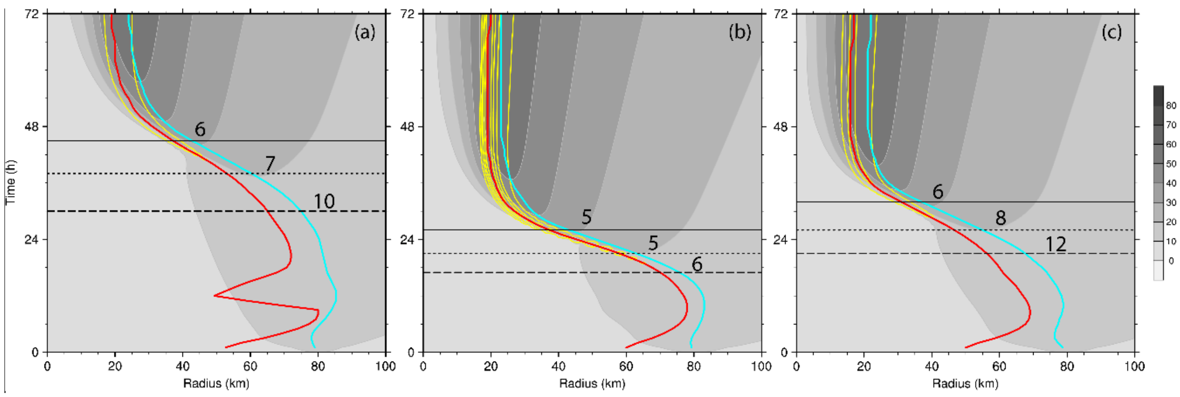

Fig. 4. Radius-time diagrams of v_1 (shaded at an interval of 10 m s^{-1}) and w_b (contoured at an interval of 2 m s^{-1} from 1 m s^{-1}) in (a) MBL, (b) SBL, and (c) FMBL. The thick red and blue curves mark the radii of maximum w_b and v_1, respectively. Long dashed, short dashed, and solid horizontal lines in each panel refer to the respective times for the storm intensity at 15, 20, and 30 m s^{-1}, respectively. The values (unit: km) denote the radial distances between the maximum w_b and v_1.

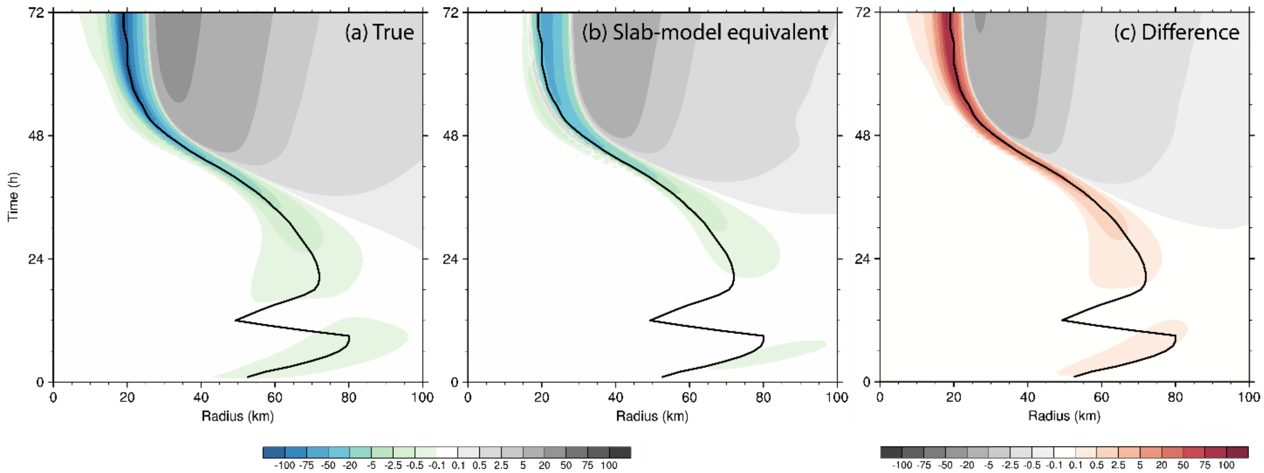

Fig. 5. Radius-time diagrams of (a) the true depth-averaged radial advection of u ($-\overline{u\partial u/\partial r}$, unit: m s^{-1} h^{-1}) and (b) the slab-model equivalent radial advection of u ($-\bar{u}\partial\bar{u}/\partial r$) in MBL. The difference $-\overline{u'\partial u'/\partial r}$ is shown in (c). The thick line in each panel denotes the location of the maximum w_b in MBL. Note that to give a better illustration, the contours are not at a constant interval.

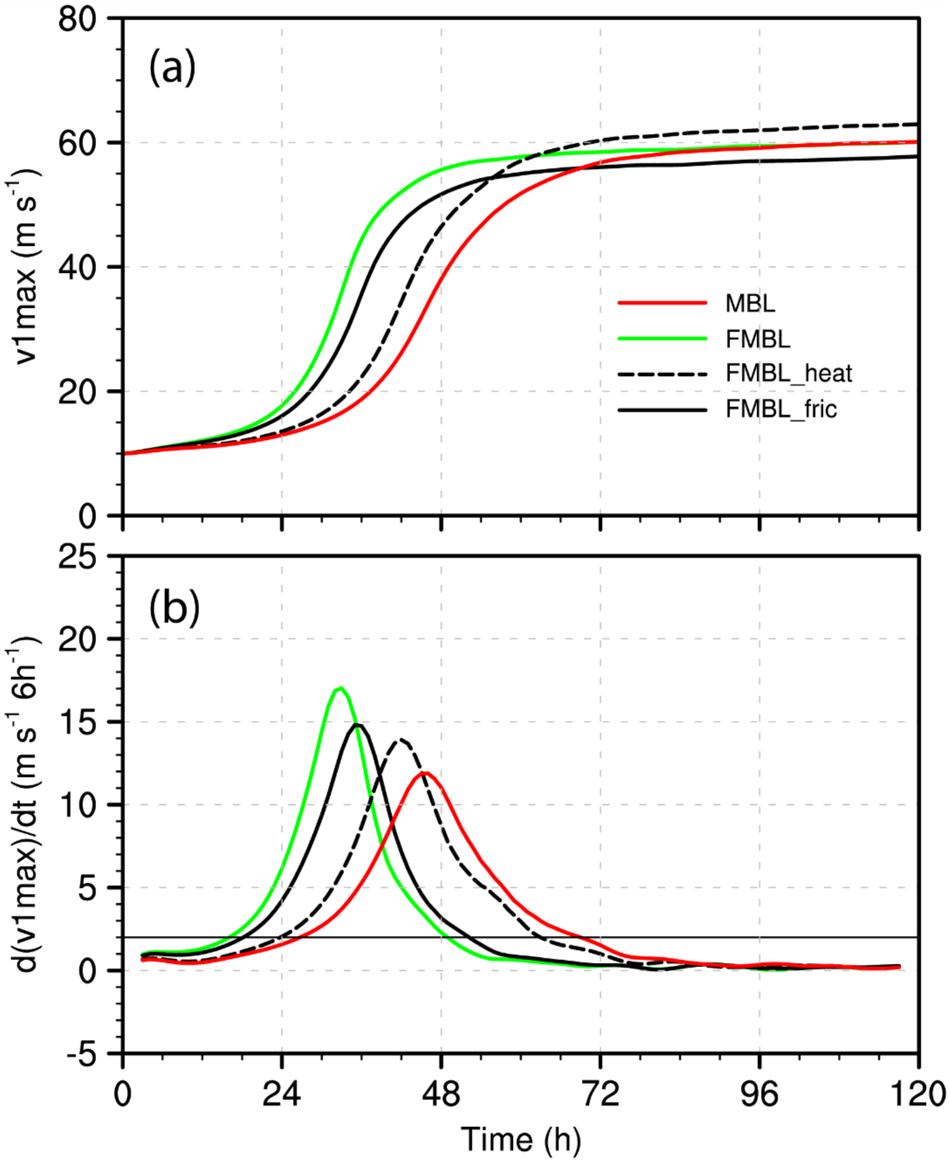

799

800 Fig. 6. Time series of (a) maximum v_1 and (b) 6-hourly intensification rate in MBL (red), FMBL

801 (green), FMBL_heat (black solid), and FMBL_fric (black dashed).

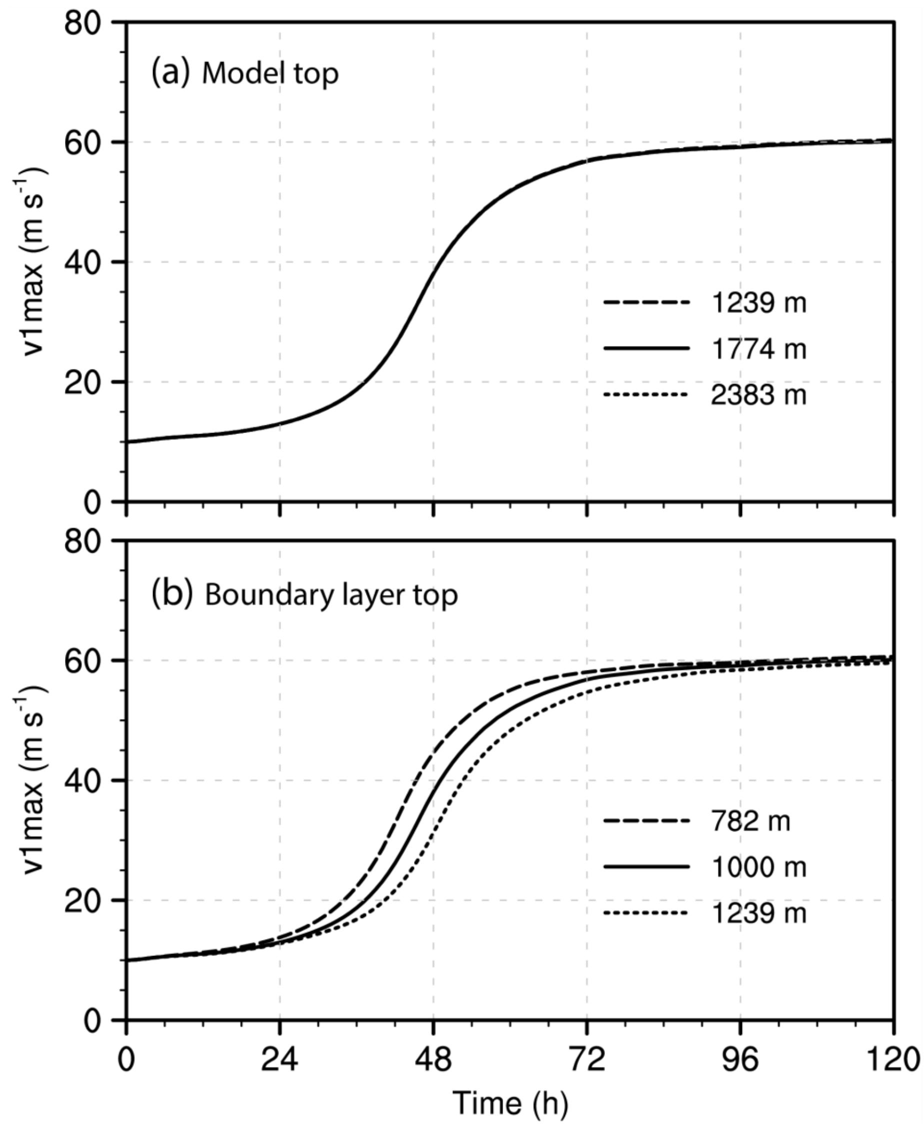

Fig. 7. (a) Time series of maximum v_1 of the storms simulated in MBL with the height of the boundary layer model at 1239 (long dashed), 1774 (solid), and 2383 m (short dashed), respectively. (b) Time series of maximum v_1 of the storms simulated in MBL with the boundary layer top (h_b) set at 782 (long dashed), 1000 (solid), and 1239 m (short dashed), respectively.

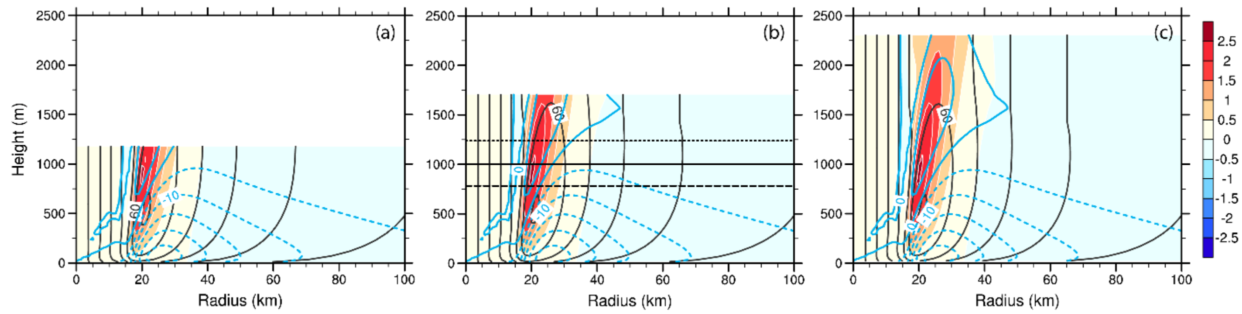

Fig. 8. Radius-height diagrams of the steady-state boundary layer winds simulated by MBL with the model height at (a) 1239, (b) 1774, and (c) 2383 m, respectively, including tangential (contoured in black at an interval of 10 m s^{-1}), radial (contoured in blue at an interval of 5 m s^{-1}), and vertical winds (shaded at an interval of 0.5 m s^{-1}). The long-dashed (782 m), solid (1000 m), and short-dashed (1239 m) horizontal lines in (b) mark the heights of the boundary layer top in the three experiments shown in Fig. 7b.

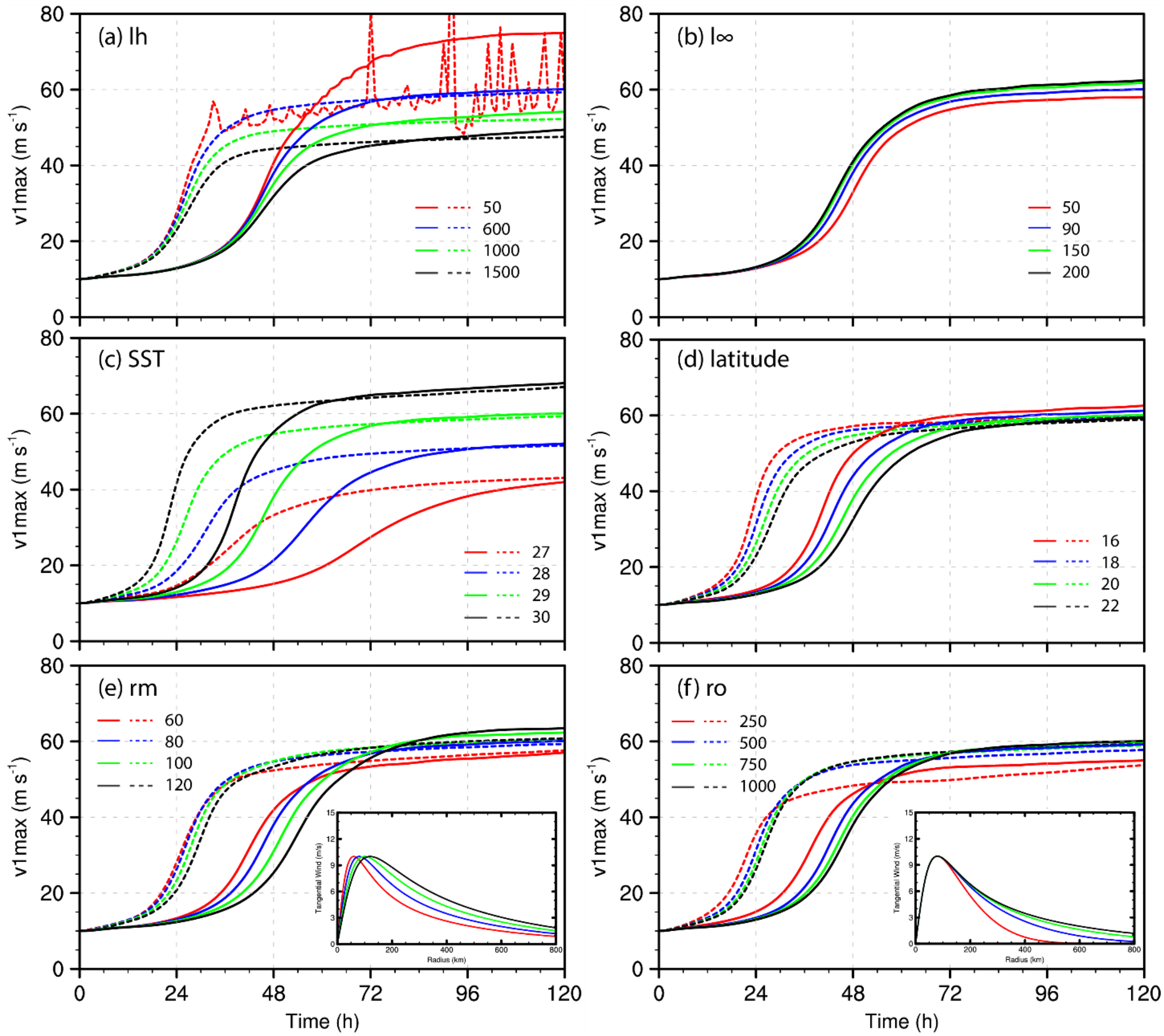

Fig. 9. Sensitivities of the simulated TC intensity evolution to (a) the horizontal mixing length (l_h, unit: m), (b) the asymptotic vertical mixing length (l_∞, unit: m), (c) sea surface temperature (SST, unit: ℃), (d) latitude (unit: degree) of the Coriolis parameter, and (e) radius of maximum wind (r_m, unit: km) and (f) decay parameter (r_o, unit: km) of the initial TC vortex in MBL (solid curves) and SBL (dashed curves). The initial wind profiles of the sensitivity experiments in (e) and (f) are shown as thumbnails.